Materials Transactions, Vol. 67, No. 5 (2026) pp. 771 to 782

Microstructural Evolution and Wear Resistance Enhancement of Electron-Beam-Fabricated Nickel Titanium Coatings on Titanium by Heat Treatment

Lei Wang[1], Masayuki Okugawa[1,2,*], Yuheng Liu[1], Ken Cho[1,2], Yuichiro Koizumi[1,2,*], Hiroyuki Y. Yasuda[1,2] and Takayoshi Nakano[1,2]

[1]*Graduate School of Engineering, The University of Osaka, Suita 565-0871, Japan*
[2]*3DPTec Integrated Center, The University of Osaka, Suita 565-0871, Japan*

We previously proposed a novel method for fabricating NiTi coatings on pure Ti surfaces using electron-beam multi-track scanning to improve wear resistance. However, electron-beam scanning coatings exhibit spatial inhomogeneity in phase and elemental distributions, which is suggested to decrease wear resistance. In the present study, we investigated the effects of heat treatment on reducing inhomogeneity and improving the performance of the coatings. As a result, the homogeneity of the electron beam (EB) scanned coatings was significantly enhanced after annealing (900°C, 10 min), and then the Ni_4Ti_3 phase precipitated in the annealed EB-scanned coatings after aging (400°C, 60 min). The results of nanoindentation show that the hardness/indentation modulus (H/E) ratio and depth recovery ratio ($\eta_{d,h}$) of the Ti-rich EB-scanned coatings increased by 27% and 21%, respectively, after annealing and aging. The H/E ratio and $\eta_{d,h}$ of the Ni-rich EB-scanned coating improved by 8% and 14%, respectively, after annealing and aging. The wear test results demonstrate that the wear rates of the two coatings decreased by 52% and 26% after annealing and aging, respectively, approaching the wear performance of bulk Nitinol.
[doi:10.2320/matertrans.MT-M2025170]

(Received December 15, 2025; Accepted February 7, 2026; Published April 25, 2026)

Keywords: *commercially pure titanium, nickel titanium coating, heat treatment, mechanical properties, wear resistance*

1. Introduction

Commercially pure titanium (CP-Ti) is widely used in biomedical [1], aerospace [2], chemical [3], marine [4], and nuclear [5] sectors due to its exceptional corrosion resistance, biocompatibility, lightweight characteristics, and high specific strength [6]. Nonetheless, its limited wear resistance restricts use in critical transmission components such as engines and pumps [7, 8]. Although alloying can improve wear resistance to some extent, it often affects bulk properties. For instance, Ti-6Al-4V exhibits a dry friction wear rate approximately 50% lower than that of CP-Ti [9, 10]. However, this enhancement remains insufficient, as alloying typically reduces ductility; the tensile elongation of Ti-6Al-4V drops to around 10%, nearly half that of CP-Ti [11].

Surface engineering provides a practical approach to enhance surface properties, such as wear resistance, while imparting new functionalities to the surface without altering bulk characteristics [12–14]. Coating [15, 16] is a prevalent surface treatment technique in this field, in which the substrate is covered with a more wear-resistant material to protect it. Among various coating materials, NiTi is particularly noteworthy due to its outstanding performance. NiTi exhibits superelasticity (SE) [17, 18], which can significantly improve wear resistance, surpassing even that of Ti-6Al-4V [19]. Additionally, NiTi is an ideal candidate for diverse coating methods, including thermal spraying [20–22], cold spraying [23, 24], and magnetron sputtering [25]. Therefore, employing NiTi coatings offers a promising strategy to address the wear resistance limitations of commercially pure titanium (CP-Ti).

*Corresponding authors, E-mail: okugawa@mat.eng.osaka-u.ac.jp, ykoizumi@mat.eng.osaka-u.ac.jp

In our previous studies [26, 27], a novel method that combines electroplating with an additive manufacturing technique [28–33], specifically EBM, was proposed for fabricating *in situ* synthesized NiTi coatings on CP-Ti substrates. The technique consists of two steps: first, electroplating a pure Ni layer onto CP-Ti; second, scanning the Ni-plate layer with an electron beam (EB). We successfully fabricated NiTi coatings on CP-Ti surfaces using multi-track scanning [27]; the optimal EB-scanned NiTi coating consisted of the superelastic *B*2-NiTi phase, which reduced the wear rate by 80% compared to CP-Ti. However, EB-scanned NiTi coatings showed issues with the elemental distribution inhomogeneity, which causes localized presence of *C*15-$NiTi_2$ phase and is suggested to limit its performance.

Heat treatment is a commonly used post-processing method for coatings such as thermal spray, cold spray, and magnetron sputtering. It promotes homogeneity in the distribution of phases in the coatings [18, 34, 35]. Furthermore, studies show that the microstructure and mechanical characteristics of additively manufactured NiTi can be optimized through heat treatment; specifically, annealing and aging processes can increase recoverable strain [36, 37] and enhance strain cycling stability in superelastic NiTi [38, 39], thereby improving wear resistance. Accordingly, heat treatment should not only homogenize the EB-scanned coatings but also further enhance their superelasticity, thereby improving wear resistance.

In the present study, the effects of heat treatment on NiTi coatings fabricated via EB scanning were examined. The coatings were subjected to thermal annealing at 900°C followed by aging at 400°C to assess changes in microstructure and wear resistance. The findings enhance the understanding of EB scanning as an innovative coating method, advancing its potential for practical applications and

informing heat treatment protocols for additively manufactured NiTi.

2. Experimental Procedure

2.1 Sample preparation

A slab of CP-Ti (99.5% purity; Nilaco, Tokyo, Japan) was sectioned into specimens measuring 25 × 25 × 10 mm^3 using electric discharge machining. A specimen with a 25 × 25 mm^2 surface area served as the working electrode. The CP-Ti specimen underwent a four-step pretreatment process: (1) mechanical grinding with SiC abrasive papers of grit sizes P120–P2400; (2) immersion in ethanol at room temperature for 5 minutes; (3) immersion in a 10 mass% HCl solution at room temperature for 5 minutes, with a 9 V DC voltage applied to facilitate the removal of surface oxides and contaminants; and (4) rinsing with ultrapure water.

A pure Ni anode with dimensions ϕ 6 × 20 mm and an area of 405 mm^2 was employed, with an interelectrode gap of 8 cm. In this study, a thicker nickel layer was required for subsequent processing, leading to the use of a nickel sulfamate solution as the plating bath. This type of bath supports high current densities and produces plated layers with reduced internal stress, making it suitable for applications requiring greater coating thickness [40]. The solution compositions and electroplating parameters, adopted from an electrochemical handbook [40], are detailed in Table 1. Electroplating was carried out for 4 hours to achieve a sufficiently thick layer. Post-deposition, the layer was ground using P120–P2000 grit SiC abrasive papers to reach a final thickness of 45 µm.

The specimens were scanned using an EB in an EBM-6LB-1 system (Mitsubishi Electric) within a helium atmosphere at a pressure of 0.5 Pa. Multi-track scanning was conducted over a 3 × 4 mm^2 area employing a serpentine pattern (see Fig. 1). The EB power was adjusted to two levels, 126 W and 138 W. The line offset was maintained at 300 µm, and the scanning speed was set to 100 mm/s. To prevent heat accumulation, a 60-second pause was incorporated into the procedure between scans.

The EB-scanned samples were subjected to annealing at 900°C for 10 minutes under a vacuum condition, followed by rapid quenching in ice water. Subsequently, the annealed specimens were aged at 400°C for 60 minutes and similarly quenched in ice water.

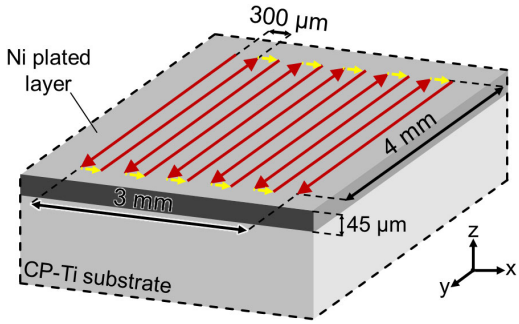

Fig. 1 Schematic of a Ni-plated CP-Ti substrate subjected to EB scanning. (online color)

2.2 Microstructure and phase analysis

The coating samples were cut perpendicular to the beam-scanning direction for cross-sectional analysis using field-emission scanning electron microscopy (FE-SEM; JSM 6500, JEOL, Japan). Elemental distributions were examined through energy-dispersive X-ray spectroscopy (EDS). Crystalline phases of the surface layer were identified using X-ray diffractometry (XRD; SmartLab SE diffractometer, Rigaku, Japan), with Cu Kα radiation and a 2 theta range from 20° to 80°, scanning in 0.01° steps. Each sample was tested three times under consistent conditions. The formation of Ni-Ti intermetallic phases was investigated by analyzing the equilibrium phase characteristics of the Ni-Ti binary alloy using Thermo-Calc Software (version 2022b) and the TCTI4 thermodynamic database for Ti alloys [41].

2.3 Nanoindentation tests

Nanoindentation tests were conducted using an ENT-1100a nanoindenter (Elionix, Japan) equipped with a Berkovich indenter to assess the indentation behavior of the EB-scanned coating. Specimen surfaces were ground with P120–P4000 grit SiC abrasive papers and polished using a 50 nm alkaline colloidal silica suspension before testing. Tests were performed at 26°C within a shielded enclosure to minimize thermal drift. For each sample, 50 evenly spaced points were selected for repeated testing under identical conditions, and the results were averaged to reduce variability. The peak load was set at 50 mN with a loading rate of 5 mN/s. A Berkovich indenter [42] with a 65.03° apex angle was used, and the contact area (A) and indentation depth (h) relationship was applied as follows:

Table 1 Composition of Ni-plating solution and plating parameters.

	Compound/Parameter	Value
Composition	$NiCl_2 \cdot 6H_2O$	0.10–0.13 mol/L
	$Ni(SO_3NH_2)_2$	1.70–1.79 mol/L
	H_3BO_3	0.49–0.73 mol/L
Parameters	Temperature	50–60 °C
	pH	3.0–5.0
	Cathodic current density	3.0 A/dm^2
	Current mode	DC plating

$$A(h) = 3\sqrt{3}\tan^2(65.03^\circ)\cdot(h+\Delta h)^2. \quad (1)$$

Here, Δh represents the indenter tip correction value determined using the Sawa–Tanaka method [43], based on indentation data from a standard fused silica sample. From these results, indentation elastic modulus (E) and hardness (H) were computed in accordance with ISO 14577-1 [44]. Regarding the detailed determination of the E value in the protocol, two steps are included in. Firstly, the reduced modulus (E_r) was calculated as follows:

$$E_r = \frac{S\sqrt{\pi}}{2\sqrt{A(h_c)}}. \quad (2)$$

Here, S is the gradient of the unloading curve on the load-displacement curve, and h_c is the contact depth between the sample and the indenter. The reduced modulus E_r reflects the elastic contributions of both the indenter and the sample. The indentation modulus of the sample is calculated by correcting for the indenter's elastic properties using the following equation:

$$E = \frac{1-(\nu_s)^2}{\frac{1}{E_r} - \frac{1-(\nu_i)^2}{E_i}}. \quad (3)$$

Here, E_i and ν_i are the indentation modulus and Poisson's ratio of the indenter. The values used in this study are 1200 GPa and 0.2 [45], respectively. The Poisson's ratio of the sample is represented by ν_s, for which the value of 0.45 for superelastic NiTi is used [46].

In indentation testing, the non-uniform strain field around the indenter causes elastic strain, plastic strain and force-induced martensitic phase transformation to occur simultaneously within the deformation zone surrounding the indenter. Consequently, the measured indentation elastic modulus in this study is an equivalent elastic modulus, combining the elastic and superelastic responses of the material.

Additionally, the depth recovery ratio ($\eta_{d,h}$) is defined as the proportion of recoverable indentation depth to the indenter displacement at maximum load [47], calculated as follows:

$$\eta_{d,h} = \frac{h_{max} - h_p}{h_{max}}, \quad (4)$$

where h_{max} and h_p are the maximum penetration depth of the indenter during the indentation tests and the permanent depth after load removal, respectively.

2.4 Sliding wear tests

Sliding wear tests were performed in accordance with ASTM G133-22 [48] using an OST3000 oscillation sliding tester (Rhesca, Japan) to assess the coatings' wear resistance. Before testing, specimen surfaces were ground with P120–P4000 grit SiC abrasive papers and polished with a 50 nm alkaline colloidal silica suspension. Tests applied a constant load (L) of 50 N using an alumina ceramic indenter, which has a diameter of 9.5 mm and a hardness of 2085 $HV_{0.1}$ [49]. Each specimen underwent 1 Hz oscillation with an 8 mm amplitude for 625 seconds, resulting in a total sliding distance of 10 meters (8 mm × 2 × 625 s). The internal tester environment was maintained at 26°C temperature and 50% relative humidity. Each specimen was tested twice under these conditions. The friction coefficient (μ) was calculated as follows:

$$\mu = \frac{F_Z}{F_T}, \quad (5)$$

where F_Z and F_T are normal and tangential loads, respectively. Both forces were measured and recorded continuously by the integrated sensor throughout the testing procedure.

Specific wear rate (W_s) is an indicator of a material's wear resistance [50]. The W_s for the specimens was determined using the following procedure:

$$W_s = \frac{V}{LD}. \quad (6)$$

The variables V, L, and D represent volume loss, applied load, and sliding distance, respectively. V was determined using a confocal laser scanning microscope following the sliding test. Surface wear was further examined through SEM imaging and EDS analysis. For comparison, a commercially available superelastic NiTi alloy (Ni 50.6 at%, Ti 49.4 at%; Seemine Keli, Lanzhou, China) and the substrate material, commercially pure titanium (CP-Ti), were also tested as control specimens.

3. Results and Discussions

3.1 Microstructure and crystallographic phase formed in the heat treated coatings

Figure 2 presents BSE images and EDS maps of the cross-sections of the as-scanned, annealed, and aged coatings. The BSE images and EDS data of as-scanned coatings are adapted from our previous study [27] for the purpose of comparison. Some dark streaks and areas (indicated by the black arrows) are visible at certain melt track junctions in Figs. 2(a1) and 2(d1). This indicates inhomogeneity in the EB-scanned coating. The dark phases in Ti-rich coating are significantly larger compared to those in the Ni-rich coating. EDS mapping data (Figs. 2(a2) and 2(d2)) show that these areas near the junctions of the melt tracks are rich in Ti and that the dark phases correspond to the $NiTi_2$ phase. As illustrated in Fig. 2(b1), the phase distribution across the cross-section of the annealed Ni-rich coating has become more homogeneous, with the dark streaks at the melt track junction (indicated by black arrows) nearly eliminated. Corresponding EDS map confirms a more uniform elemental distribution. Similarly, the annealed Ti-rich coating shown in Fig. 2(e1) exhibits markedly improved uniformity compared to the as-scanned coating. The dark areas at the melt track junction have noticeably diminished, and regions with Ti concentrations reaching 66 at% in the EDS map have significantly reduced. As can be seen in Figs. 2(b1), 2(c1), 2(e1), and 2(f1), the cross-sectional morphology of the annealed and aged coatings differs minimally from that of the annealed coatings. This is due to the low diffusion coefficients of Ni and Ti within the NiTi phase at an ageing temperature of 400°C, resulting in a short diffusion distance of less than 0.1 μm [50]. Consequently, solid-state diffusion does not substantially alter the cross-sectional morphology.

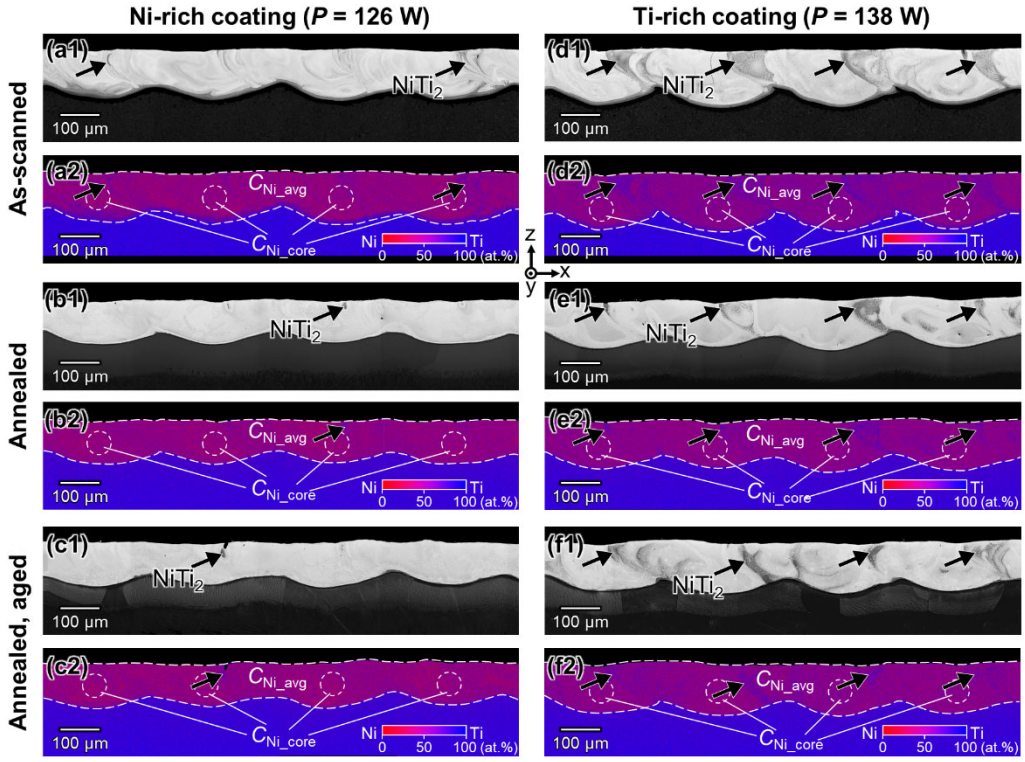

Fig. 2 BSE images and EDS mapping of the cross section of four melt tracks in (a)–(c) Ni-rich EB-scanned coatings ($P = 126$ W) and (d)–(f) Ti-rich EB-scanned coatings ($P = 138$ W) undergone different heat treatment states. (a), (d) As-scanned coatings. (b), (e) Annealed coatings. (c), (f) Annealed and aged coatings. The black arrows in the BSE image indicate the dark streaks at the junctions of the melt tracks. The BSE images and EDS data of as-scanned coatings are adapted from our previous study [27]. (online color)

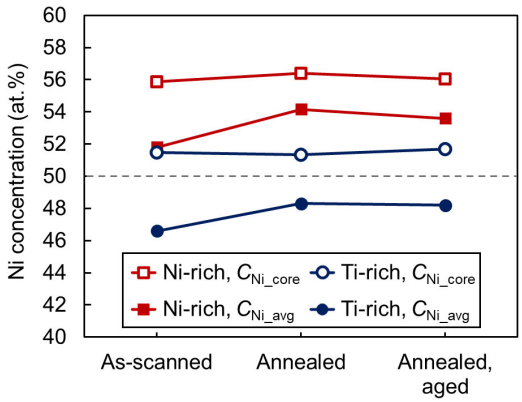

Fig. 3 Variation in the average Ni concentrations (C_{Ni_avg}, at%) and the core Ni concentration of melt track (C_{Ni_core}, at%) in the EB-scanned coatings under different heat treatment states. The area selected for calculating C_{Ni_avg} and C_{Ni_core} are shown in Fig. 2. (online color)

Figure 3 shows the changes in the average Ni concentration (C_{Ni_avg}, at%) and the core Ni concentration of melt track (C_{Ni_core}, at%) within the EB-scanned coating during heat treatment. The regions selected for calculating these two characteristic values are indicated in Fig. 2. The value of C_{Ni_avg} is calculated using EDS data across all regions of each coating cross-section. The value of C_{Ni_core} is calculated from EDS data acquired within a circular area of approximately 60 μm in diameter at the core of the melt tracks in the coating. It can be observed that C_{Ni_avg} increases in both Ni-rich and Ti-rich coatings after annealing, while remaining generally unchanged after aging. However, C_{Ni_core} did not exhibit a trend similar to C_{Ni_avg}, showing no significant change after annealing or aging. This indicates that although changes occurred in the coating's average composition, no large-scale solid-state diffusion altering the coating's matrix composition occurred during annealing and aging.

Figure 4 shows magnified BSE images of the as-scanned, annealed, and aged EB-scanned coatings, alongside EDS depth profiles. The BSE images and EDS data of as-scanned coatings are adapted from our previous study [27] for the purpose of comparison. As discussed earlier, the $NiTi_2$ phase at the melt track junctions of the as-scanned state coatings can also be observed in Figs. 4(a4), and 4(d4) (indicated by black arrow). In the Ni-rich coating (Fig. 4(a4)), the $NiTi_2$ phase are elongated, exhibiting a width of less than 1 μm but extending tens of micrometers in length. The $NiTi_2$ phases are larger in the Ti-rich coating (Fig. 4(d4)), exceeding 10 μm in width at their widest points. Additionally, Fig. 4(d3) reveals a $NiTi_2$ phase branch protrudes from the melt track boundary into the interior of the Ti-rich coating. After annealing, as shown in Fig. 4(b4), the $NiTi_2$ phase in the Ni-rich coating is significantly reduced, with the remaining phase transformed into a grain approximately 2 μm wide and 10 μm long. The $NiTi_2$ phase at the melt track junction in the Ti-rich coating also markedly decreased after annealing (Fig. 4(e4)). Similarly, the $NiTi_2$ phase branch protruded from the melt track boundary also disappears (Fig. 4(e3)). These results suggest that the $NiTi_2$ precipitations which decrease the plasticity, toughness and wear resistance of the EB-scanned coating are mitigated after annealing.

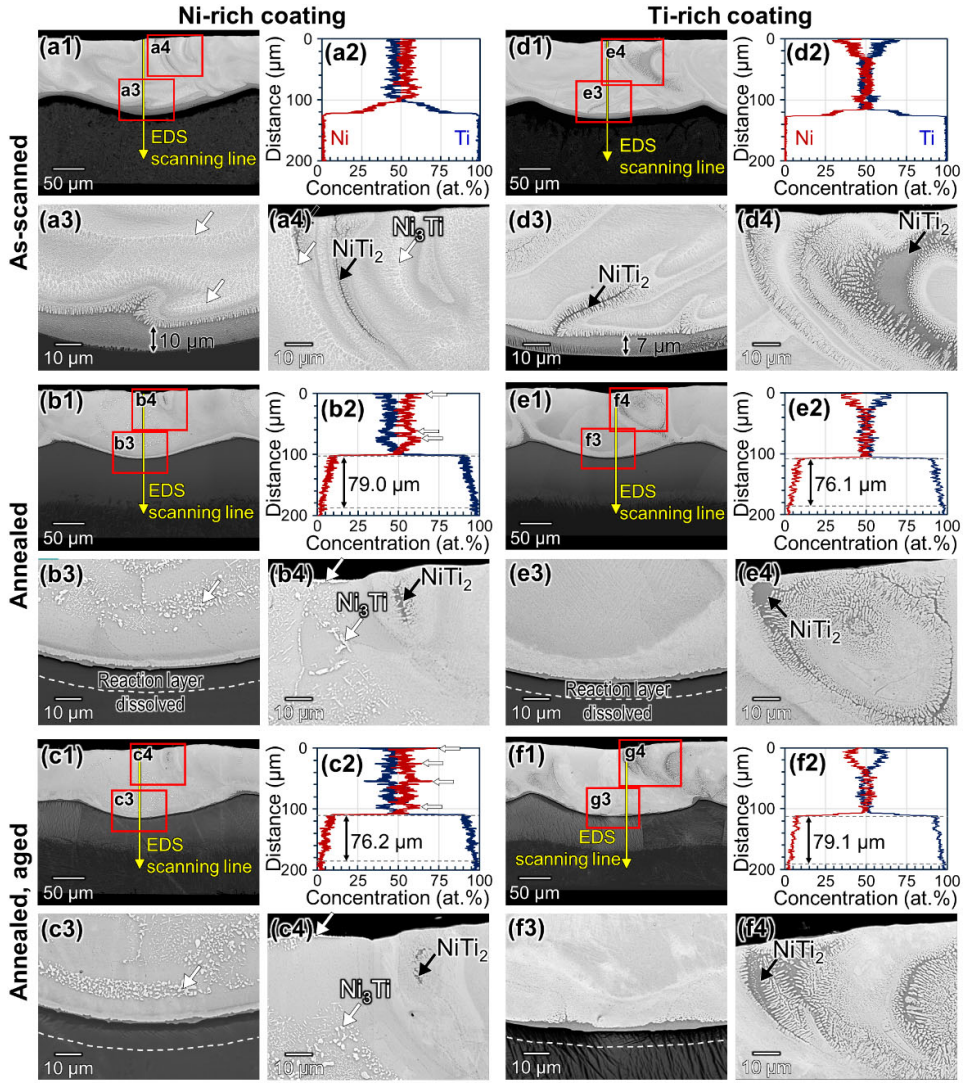

Fig. 4 Magnified BSE images and EDS depth profile of (a)–(c) Ni-rich EB-scanned coatings and (d)–(f) Ti-rich EB-scanned coatings in different heat treatment states. (a), (d) As-scanned coatings. (b), (e) Annealed coatings. (c), (f) Annealed and aged coatings. The BSE images and EDS data of as-scanned coatings are adapted from our previous study [27]. (online color)

Moreover, as can be seen in Figs. 4(a3) and 4(d3), a layer of dark phase is present at the boundary of the Ni-rich and Ti-rich coatings in their as-scanned state. EDS data in Figs. 4(a2) and 4(d2) show that layer is primarily composed of the $NiTi_2$ phase. It is suggested that this layer is a reaction layer formed through reaction between the CP-Ti substrate and liquid metal in the melt pool during EB scanning. As can be seen in Figs. 4(b3) and 4(e3), the $NiTi_2$ phase reaction layer has disappeared after annealing. Additionally, EDS profiles (Figs. 4(a2), 4(b2), 4(d2) and 4(e2)) reveal that the Ni concentration within the coating remains almost unchanged after annealing, which is consistent with the C_{Ni_core} trend shown in Fig. 3. Meanwhile, the substrate, which contained no Ni before annealing, develops a Ni-gradient layer approximately 80 μm thick post-annealing, with Ni concentration decreasing vertically. This indicates that the $NiTi_2$ phase in the reaction layer has dissolved in the Ti substrate during the annealing. This occurs because Ni diffusion in the Ni-Ti system occurs almost exclusively in one direction, from Ni-rich to Ti-rich regions [51]. Furthermore, the integrated diffusion coefficient calculated using the Wagner method of the $NiTi_2$ phase, $3.53 \times 10^{-12}\,m^2/s$, is significantly higher than that of the NiTi phase, $18.1 \times 10^{-15}\,m^2/s$, and the Ni_3Ti phase, $6.2 \times 10^{-15}\,m^2/s$ [51]. This also explains why the C_{Ni_avg} of the coating increases after annealing: the region used to calculate the C_{Ni_avg} of the as-scanned coating includes the NiTi matrix and the $NiTi_2$ reaction layer, whereas the region used to calculate the C_{Ni_avg} of the annealed coating includes only the NiTi matrix. This indicates that the coating composition did not change significantly due to the solid diffusion during the heat treatments. Thus, all microstructural changes are almost attributed to diffusion within the coating itself.

Reticular bright regions indicated by white arrows in Figs. 4(a3) and 4(a4) are distributed throughout the as-scanned Ni-rich coating, which are suggested to be the Ni_3Ti phase. In the annealed Ni-rich coating (Figs. 4(b3) and 4(b4)), the reticular Ni_3Ti phases observed in the as-scanned state have grown into a needle-like or granular shape. EDS profile (Fig. 4(b2)) reveals abrupt increases in Ni concentration where the scan line traverses these Ni_3Ti phases (indicated by white arrows). The growth of the Ni_3Ti phase

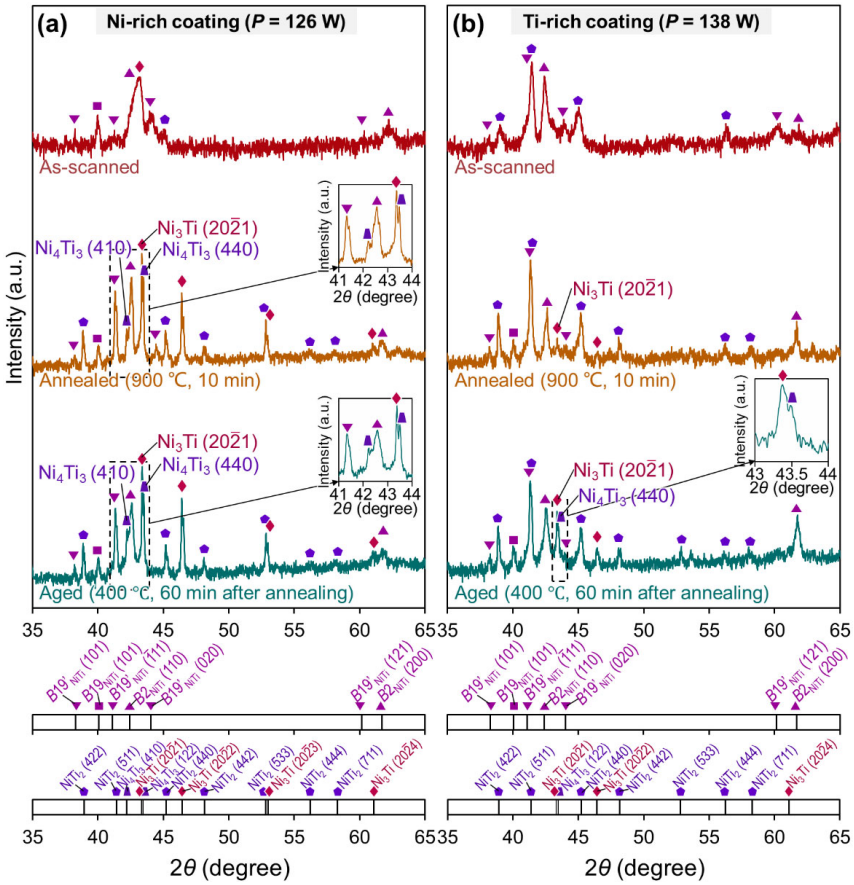

Fig. 5 XRD patterns of EB-scanned coatings under the state of as-scanned, annealed, annealed and aged. The scanning conditions for the as-scanned coatings are as follows: (a) $P = 126$ W, resulting in a Ni-rich coating; and (b) $P = 138$ W, resulting in a Ti-rich coating. The data of as-scanned coatings are adapted from our previous study [27]. (online color)

results from Ostwald ripening within the coating during annealing [52]. However, as shown in Figs. 4(c) and 4(f), neither the Ni-rich coating nor the Ti-rich coating exhibited any microstructural or elemental distribution changes observable at the micrometer scale after aging compared to the annealed state.

Figure 5 shows the XRD patterns of as-scanned, annealed, and aged coatings. The data of the as-scanned coating presented here were reported in our previous study [27]. The EB-scanned coatings predominantly consist of the NiTi phase. Notably, the elevated Ni concentration in the Ni-rich coating leads to the prominent presence of the Ni_3Ti phase alongside the *B*2-NiTi phase in the as-scanned Ni-rich coating shown in Fig. 5(a). The Ni_3Ti peaks become narrower and more intense in the XRD profile of the annealed Ni-rich coating, confirming the growth of the Ni_3Ti grains observed in Figs. 4(b3) and 4(b4). Furthermore, after annealing, peaks corresponding to the metastable Ni_4Ti_3 phase also appear, which is not observed under SEM in Fig. 4. The Ni_4Ti_3 phase is suggested to be formed by interfacial reactions between Ni_3Ti, NiTi, and $NiTi_2$ phases, similar to observations in Ni-Ti diffusion couples reported by Babaei-Dehkordi *et al.* [51]. As shown in the XRD patterns of the aged Ni-rich coating (Fig. 5(a)), the peak intensity of Ni_4Ti_3 increased after ageing, indicating greater precipitation of the Ni_4Ti_3 phase. The Ni_4Ti_3 precipitates assist the stress-induced martensitic transformation and suppress plastic slip in the *B*2-NiTi phase, resulting in stabilized and superior superelasticity [36–39]. These phases also contribute to precipitation hardening and increased mechanical strength of the coating [53].

The XRD pattern of the as-scanned Ti-rich coating shown in Fig. 5(b) indicates a significant presence of *B*19′-NiTi phase alongside $NiTi_2$ phase. After annealing, low-intensity peaks at $2\theta = 43.39°$ for Ni_3Ti appear. After aging, a notable increase in Ni_3Ti peak intensity and the appearance of Ni_4Ti_3 peaks are observed, indicating the precipitation of Ni_3Ti and Ni_4Ti_3 phases. Although the overall composition of the coating is Ti-rich, the core regions are slightly Ni-rich, as shown in Fig. 3, which allows the precipitation of these Ni-rich phases. These precipitates are suggested to enhance mechanical properties, as in Ni-rich coatings.

3.2 Effects of heat treatment on mechanical properties

Figure 6 shows the results of nanoindentation tests on Ni-rich and Ti-rich EB-scanned coatings under different heat-treatment conditions. The nanoindentation results of as-scanned coatings, superelastic Nitinol (SE-NiTi) and the substrate material, CP-Ti were reported in our previous study [27] and are reused here to compare with the heat-treated coatings. Figure 6(a) shows the load-displacement curves from nanoindentation tests for the coatings, SE-NiTi and CP-Ti. To avoid overlapping curves, only the Ti-rich coating data are presented. The maximum indenter penetration depth

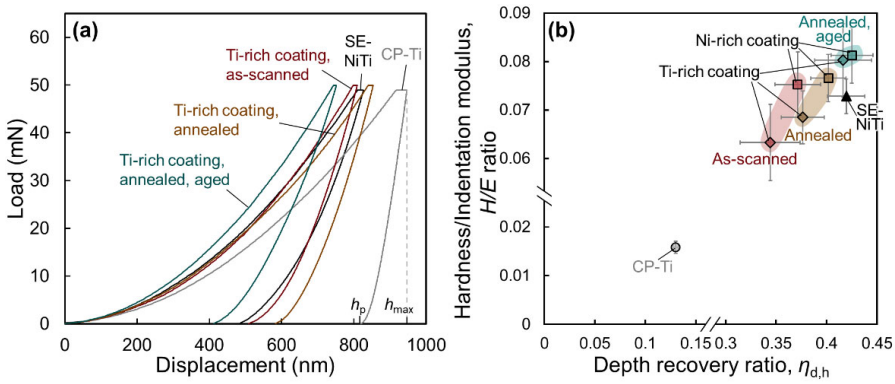

Fig. 6 (a) Load-displacement curve and (b) plot of hardness/indentation modulus ratio (H/E ratio) versus depth recovery ratio ($\eta_{d,h}$) of CP-Ti, superelastic Nitinol (SE-NiTi) and EB-scanned coatings at various heat treatment states. The data of as-scanned coatings, SE-NiTi and CP-Ti are adapted from our previous study [27]. (online color)

during loading (h_{max}) and the permanent indentation depth after unloading (h_p) can be inferred from these curves. Traditionally, higher hardness has generally been considered to indicate improved wear resistance [54, 55]. However, several recent studies have suggested that the hardness/indentation modulus ratio (H/E ratio) [56–58] and the depth recovery ratio ($\eta_{d,h}$) [59–61] are better correlated with wear resistance than hardness alone.

According to the classical wear theory, one significant cause of wear is localized fracture due to severe plastic deformation of the material surface [62]. Materials with higher H/E ratio and higher $\eta_{d,h}$ values exhibit a greater proportion of recoverable elastic deformation and a smaller proportion of irreversible plastic deformation during surface contact [63, 64]. This also implies reduced susceptibility to wear, i.e. superior wear resistance. While a significant proportion of NiTi alloy's recoverable deformation originates from stress-induced martensitic phase transformation (superelastic deformation) rather than elastic stretching of atomic bonds (elastic deformation), the aforementioned description of how H/E ratio and $\eta_{d,h}$ influence wear resistance primarily considers whether surface deformation is recoverable rather than the underlying deformation mechanism. Therefore, this mechanism of influence on wear resistance is suggested to remain valid in superelastic NiTi alloys. Therefore, the H/E ratio and $\eta_{d,h}$ can be considered more reliable indicators of wear resistance in this study.

Figure 6(b) shows a H/E ratio versus $\eta_{d,h}$ plot for the EB-scanned coatings, SE-NiTi and CP-Ti. The high H/E ratio and $\eta_{d,h}$ of SE-NiTi, as well as its superior wear resistance, originate from its superelasticity [19, 65]. The H/E ratio and $\eta_{d,h}$ of EB-scanned coatings before heat treatment are higher than those of CP-Ti, but slightly lower than those of SE-NiTi. However, after annealing and aging, the coating's H/E ratio exceeded that of SE-NiTi, and their $\eta_{d,h}$ became almost identical to that of SE-NiTi. This indicates that the superelasticity and wear resistance of EB-scanned coatings were enhanced by annealing and aging. Eventually, the heat-treated coatings achieved a level of wear resistance comparable to that of SE-NiTi. Moreover, in the as-scanned state, the Ni-rich coating has a higher H/E ratio and $\eta_{d,h}$ than the Ti-rich coating. Following each heat treatment stage, the increase in the Ni-rich coating was relatively minor, whereas the increase in the Ti-rich coating was more pronounced. Consequently, after annealing and aging, the Ti-rich and Ni-rich coatings were almost identical in H/E ratio and $\eta_{d,h}$. These observations confirm that annealing homogenizes the coating, while aging promotes precipitation of the Ni_4Ti_3 phase, collectively enhancing wear resistance. Furthermore, this demonstrates that annealing and aging can narrow the performance gap between Ni-rich and Ti-rich coatings. If applied to large-scale coating production, this technique could help mitigate performance inconsistencies caused by regional variations in coating composition.

Figures 7(a) and 7(b) compare the parameters H/E ratio, H, and E of EB-scanned and heat-treated coatings with other materials such as superelastic Nitinol (SE-NiTi) [19, 56, 60, 66], structural metal (SM) [19, 56, 66–74], wear resistant (WR) coating [75–78], and the NiTi coatings from other studies [28, 79]. Commonly used SMs have hardness in the range 1–10 GPa and indentation moduli of approximately 100–300 GPa. WR-coatings are typically used for surface protection of SMs, and their hardness and H/E ratios are higher than those of most SMs. The H/E ratios of the other NiTi coatings, although higher than those of the SMs, are still lower than the average of the WR-coatings. Although SE-NiTi does not exhibit a higher H than SMs, WR coatings or other NiTi coatings, its lower E gives it a considerably higher H/E ratio. The H/E ratio of the EB-scanned coatings in this study reached or even exceeded the average level of SE-NiTi before heat treatment. This makes their H/E ratio higher than that of all SMs, WR-coatings, and other NiTi coatings. Although the H value of the EB-scanned coatings increased only slightly after annealing and aging, their H/E ratio exceeded that of all SE-NiTi coatings because the E value remained essentially unchanged after heat treatment.

Figure 7(c) also shows a comparison of the depth recovery ratio ($\eta_{d,h}$) for different materials. The results show that WR coatings exhibit a higher $\eta_{d,h}$ than the average level of SMs. However, even the highest $\eta_{d,h}$ for either material only reaches 0.3. The $\eta_{d,h}$ of all SE-NiTi, however, is greater than 0.3, meaning it is higher than that of all SMs and WR-coatings. This difference arises from the superelastic properties of SE-NiTi, which enable a high reversible strain exceeding the elastic strain limit of conventional metals [17, 18], leading to significantly higher $\eta_{d,h}$ values. Although

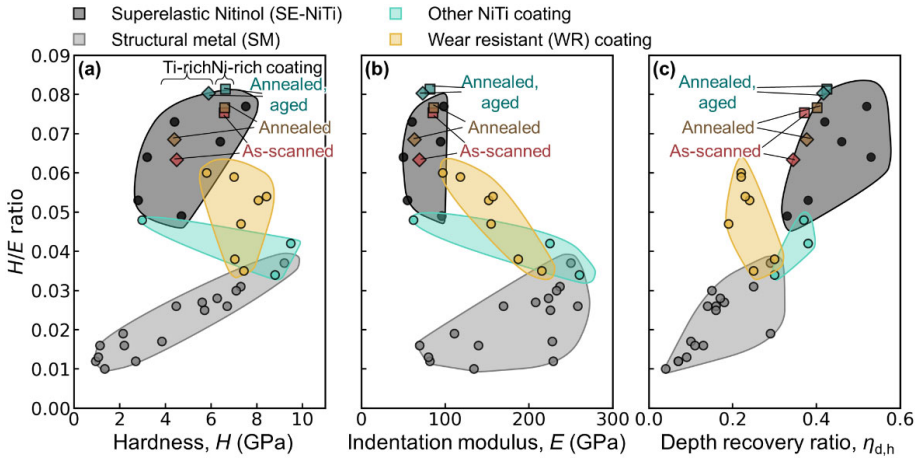

Fig. 7 Comparison of the indentation properties among the EB-scanned heat-treated coatings in the present study, superelastic NiTi [19, 50, 54, 60], structural metal [19, 50, 60–68], wear resistant coating [69–72], and other NiTi coating [28, 73]. Plot of H/E ratio vs. (a) hardness (H), (b) indentation modulus (E), and (c) depth recovery ratio ($\eta_{d,h}$). This figure is a reproduction of "Fig. 9" from our published paper [27], reproduced with permission. (online color)

the $\eta_{d,h}$ values of other NiTi coatings are higher than those of SMs and WR-coatings, they only reach the minimum level of SE-NiTi. The EB-scanned coating in this study was at the same level as other NiTi coatings before heat treatment. However, following annealing and aging treatment, the $\eta_{d,h}$ of the EB-scanned coating surpassed that of the other NiTi coatings, aligning with the lower to middle range of the SE-NiTi.

3.3 Improvement of wear resistance by heat treatment

Figure 8 shows the results of the sliding wear test for CP-Ti, superelastic Nitinol (SE-NiTi), and EB-scanned coatings in various heat treatment states. The wear test results of as-scanned coatings, superelastic Nitinol (SE-NiTi), and the substrate material, CP-Ti, were reported in our previous study [27] and are reused here to compare with the heat-treated coatings. The results demonstrate that the specific wear rate (W_s) of the EB-scanned coating before heat treatment is notably lower than that of CP-Ti, but still slightly higher than that of SE-NiTi. Following annealing and aging treatment,

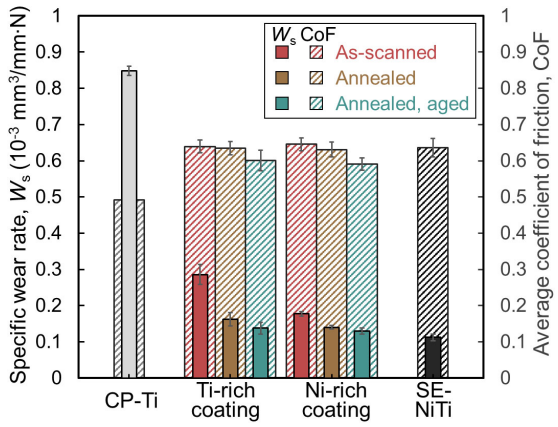

Fig. 8 Comparison of specific wear rate (W_s) and coefficient of friction (CoF) of CP-Ti and superelastic Nitinol (SE-NiTi) with EB-scanning coatings at various heat treatment states. The data of as-scanned coatings, CP-Ti and SE-NiTi are adapted from our previous study [27]. (online color)

the W_s of both the Ti-rich and the Ni-rich coatings decreased significantly. Notably, the W_s of the Ti-rich coating decreased by 51.8% after annealing and aging, compared to the as-scanned coating, while the W_s of the Ni-rich coating decreased by 26.5%. Both values approached that of SE-NiTi. This indicates that heat treatment significantly enhances the wear resistance of EB-scanned coatings, achieving wear resistance nearly equivalent to SE-NiTi. Conversely, the coefficient of friction (CoF) for CP-Ti in sliding friction tests was 0.49; all EB-scanned coatings and SE-NiTi, however, exhibited CoF values of 0.6–0.7, which are significantly higher than those of CP-Ti. Interestingly, the CoF of the annealed and aged EB-scanned coating decreased markedly compared to the as-scanned coating, dropping from 0.64 to 0.60.

Figure 9 shows the worn surfaces of CP-Ti, SE-NiTi, and EB-scanned coatings in all heat treatment states. Plate-like debris (indicated by white arrows) can be seen adhering to the worn surfaces of SE-NiTi and all EB-scanned coatings. However, no such debris is present on the CP-Ti wear surface. Corresponding EDS mapping images reveal that these particles contain aluminium, indicating that they originated from the aluminium oxide ceramic indenter and adhered to the surfaces of the SE-NiTi and EB-scanned coatings. This is due to adhesive wear [62] on the alumina indenter side, which transfers alumina debris from the indenter to the SE-NiTi and EB-scanned coatings. This also explains why their friction coefficients are higher, but their W_s are significantly lower.

Figure 10 shows magnified images of the wear surfaces of EB-scanned coatings in various heat treatment states. The worn surfaces of the as-scanned coatings (Figs. 10(a) and 10(c)) exhibit deep grooves (indicated by black arrows). The grooves on the Ni-rich surface are shorter and more discontinuous than those on the Ti-rich surface, which are longer, deeper, and wider. Figures 10(b) and 10(d) show that the number of deep grooves on the annealed coating's worn surface has decreased, with a significant reduction in both width and depth. Figures 10(c) and 10(e) show that the grooves on the worn surface of the coating after annealing

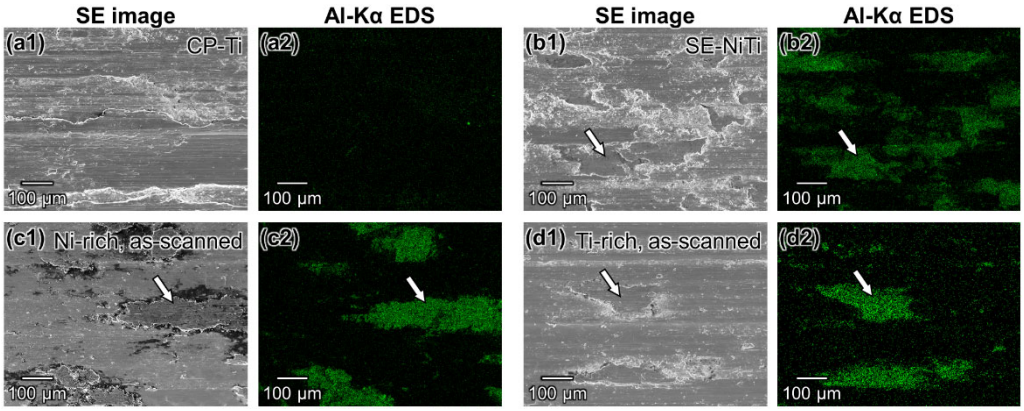

Fig. 9 SE images and Al-Kα EDS mapping of the worn surface on (a) CP-Ti substrate, (b) superelastic Nitinol (SE-NiTi), (c) as-scanned Ni-rich coating, (d) as-scanned Ti-rich coating. (online color)

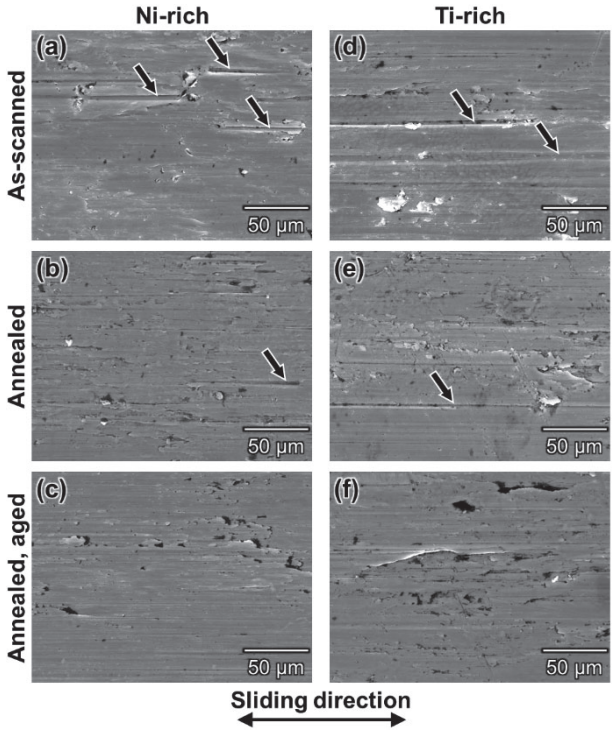

Fig. 10 Magnified SE images of worn surface on (a) as-scanned Ni-rich coating, (b) annealed Ni-rich coating, (c) annealed and aged Ni-rich coating, (d) as-scanned Ti-rich coating, (e) annealed Ti-rich coating, (f) annealed and aged Ti-rich coating. The black arrows indicate the deep grooves.

and aging became fine and uniform with no individual deep grooves present. This indicates that, following heat treatment, the increased hardness/indentation modulus ratio (H/E) and depth recovery ratio ($\eta_{d,h}$) of the coating make it more difficult for abrasive particles to plow through the surface during sliding friction, thereby reducing abrasive wear. This also explains the decrease in CoF after heat treatment.

Figure 11 shows the correlation between W_s and H, the H/E ratio and the $\eta_{d,h}$ value for CP-Ti, SE-NiTi and EB-scanned coatings in various heat treatment states. As can be seen in Fig. 11(a), there is a weak negative correlation between W_s and H in these materials, with a coefficient of determination (R^2) of 0.59. Conversely, Figs. 11(b) and 11(c) show that W_s exhibits a clear linear negative correlation with both the H/E ratio ($R^2 = 0.97$) and with the $\eta_{d,h}$ ($R^2 = 0.98$). This aligns with the findings of other relevant studies cited in Section 3.2, which confirm that the H/E ratio and $\eta_{d,h}$ are more reliable indicators of wear resistance than the H alone.

4. Conclusion

This study aims to improve the properties of the NiTi coatings scanned with an EB and fabricated in the previous study by applying heat treatment methods such as annealing and aging. Ti-rich and Ni-rich EB-scanned coatings were first annealed at 900°C for 10 minutes, followed by aging at 400°C for 60 minutes. The effects of the heat treatment on the performance of the coatings were evaluated by analyzing the phase composition, cross-sectional morphology, microstructure, indentation properties and friction-wear properties before and after the treatment. The key findings and conclusions are as follows:

(1) Annealing reduced the volume fraction and modified the morphology of the $C15$-$NiTi_2$ phase, achieving homogenization. Subsequent aging after annealing promotes precipitation of the Ni_4Ti_3 phase in the EB-scanned coating, thereby enhancing superelasticity and precipitation hardening.

(2) Annealing and ageing both significantly enhanced the hardness/indentation modulus (H/E) ratio and the depth recovery ($\eta_{d,h}$) ratio of EB-scanned coatings. Notably, the differences between the Ni-rich and Ti-rich coatings are significantly reduced after annealing and ageing, with the properties of both approaching those of superelastic Nitinol.

(3) Annealing and ageing markedly improved the wear resistance of EB-scanned coatings while reducing their friction coefficient. After annealing and ageing, the disparity in wear rates between the two coatings was eliminated, resulting in wear resistance comparable to that of superelastic Nitinol.

(4) Annealing and ageing treatments can improve the performance of EB-scanned NiTi coatings, bringing them up to the same level as bulk Nitinol. Therefore, these coatings show potential for use as wear- or erosion-resistant layers in medical implants and aerospace components.

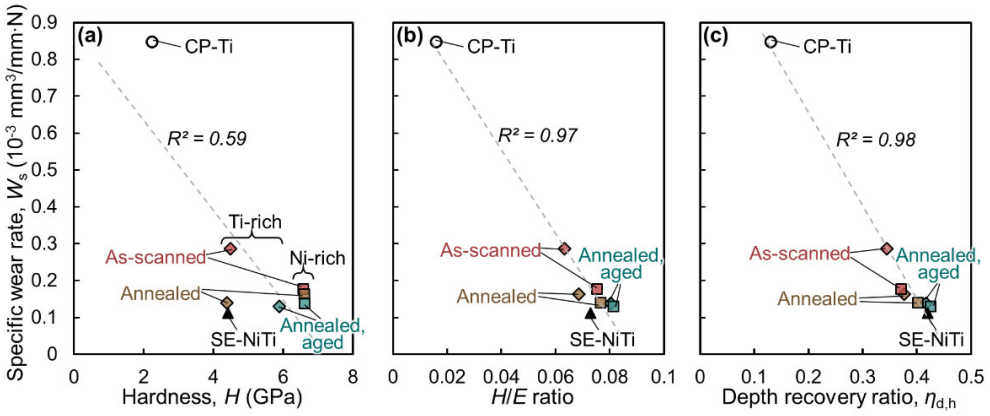

Fig. 11 Plot of specific wear rate (W_s) versus (a) hardness (H), (b) H/E ratio and (c) depth recovery ratio ($\eta_{d,h}$) of CP-Ti, superelastic Nitinol (SE-NiTi) and EB-scanned coatings at various heat treatment states. The data of as-scanned coatings, CP-Ti and SE-NiTi are adapted from our previous study [27]. (online color)

Acknowledgments

This study was partly supported by JSPS KAKENHI (Grant Numbers 21H05018, 21H05193, and 22J10955) and CREST Nanomechanics: Elucidation of macroscale mechanical properties based on understanding nanoscale dynamics for innovative mechanical materials (Grant Number: JPMJCR2194) from the Japan Science and Technology Agency (JST).

REFERENCES

[1] F.A. Shah, M. Trobos, P. Thomsen and A. Palmquist: Commercially pure titanium (cp-Ti) versus titanium alloy (Ti6Al4V) materials as bone anchored implants — Is one truly better than the other?, Mater. Sci. Eng. C **62** (2016) 960–966.

[2] R.R. Boyer: An overview on the use of titanium in the aerospace industry, Mater. Sci. Eng. A **213** (1996) 103–114.

[3] J.R.P. Jorge, V.A. Barão, J.A. Delben, L.P. Faverani, T.P. Queiroz and W.G. Assunção: Titanium in dentistry: Historical development, state of the art and future perspectives, J. Indian Prosthodont. Soc. **13** (2013) 71–77.

[4] I.V. Gorynin: Titanium alloys for marine application, Mater. Sci. Eng. A **263** (1999) 112–116.

[5] A. Kumar, M.K. Mahto, V.S. Rana, M. Vashista and M.Z.K. Yusufzai: Investigation of microstructure evolution and mechanical properties of gas tungsten arc welded dissimilar titanium (CP-Ti/Ti–6Al–4V) alloys, Proc. Inst. Mech. Eng. Part E J. Process Mech. Eng. **237** (2023) 1819–1831.

[6] G. Welsch, R. Boyer and E.W. Collings: *Materials Properties Handbook: Titanium Alloys*, (ASM International, Netherlands, 1993).

[7] Y. Qin, L. Geng and D. Ni: Dry sliding wear behavior of extruded titanium matrix composite reinforced by in situ TiB whisker and TiC particle, J. Mater. Sci. **46** (2011) 4980–4985.

[8] H. Attar, K.G. Prashanth, A.K. Chaubey, M. Calin, L.C. Zhang, S. Scudino and J. Eckert: Comparison of wear properties of commercially pure titanium prepared by selective laser melting and casting processes, Mater. Lett. **142** (2015) 38–41.

[9] P. La, J. Ma, Y.T. Zhu, J. Yang, W. Liu, Q. Xue and R.Z. Valiev: Dry-sliding tribological properties of ultrafine-grained Ti prepared by severe plastic deformation, Acta Mater. **53** (2005) 5167–5173.

[10] G. Straffelini and A. Molinari: Mild Sliding Wear of Fe–0.2%C, Ti–6%Al–4%V and Al-7072: A comparative study, Tribol. Lett. **41** (2011) 227–238.

[11] Y. Harada, Y. Ishida, D. Miura, S. Watanabe, H. Aoki, T. Miyasaka and A. Shinya: Mechanical properties of selective laser sintering pure titanium and Ti-6Al-4V, and its anisotropy, Materials **13** (2020) 5081.

[12] M. Mozetič: Surface Modification to Improve Properties of Materials, Materials **12** (2019) 441.

[13] M.S. Safavi, J. Khalil-Allafi and L. Visai: Improved osteogenic activity of NiTi orthopedic implant by HAp-Nb2O5 composite coatings: Materials and biological points of view, Biomater. Adv. **150** (2023) 213435.

[14] M.S. Safavi and A. Rasooli: The positive contribution of Cr2O3 reinforcing nanoparticles to enhanced corrosion and tribomechanical performance of Ni–Mo alloy layers electrodeposited from a citrate-sulfate bath, J. Mater. Res. Technol. **28** (2024) 865–878.

[15] H. Bai, L. Zhong, L. Kang, J. Liu, W. Zhuang, Z. Lv and Y. Xu: A review on wear-resistant coating with high hardness and high toughness on the surface of titanium alloy, J. Alloy. Compd. **882** (2021) 160645.

[16] H. Wang, G. Gao, Y. Ma, H. Zhao, B. Bhushan and J. Tong: Wear Properties of Self-Fluxing Ni60A–AlMgB14 Composite Coating Fabricated by Plasma Spraying, Mater. Trans. **63** (2022) 63–68.

[17] H. Tobushi, K. Tanaka, T. Hori, T. Sawada and T. Hattori: Pseudoelasticity of TiNi shape memory alloy: Dependence on maximum strain and temperature, JSME Int. J. Ser Mech. Mater. Eng. **36** (1993) 314–318.

[18] L. Hou and D.S. Grummon: Transformational superelasticity in sputtered titanium-nickel thin films, Scr. Metall. Mater. **33** (1995) 989–995.

[19] C. Zhang and Z.N. Farhat: Sliding wear of superelastic TiNi alloy, Wear **267** (2009) 394–400.

[20] H. Hiraga, T. Inoue, H. Shimura and A. Matsunawa: Cavitation erosion mechanism of NiTi coatings made by laser plasma hybrid spraying, Wear **231** (1999) 272–278.

[21] B. Swain, S. Mantry, S.S. Mohapatra, S.C. Mishra and A. Behera: Investigation of tribological behavior of plasma sprayed NiTi coating for aerospace application, J. Therm. Spray Technol. **31** (2022) 2342–2369.

[22] M. Bram, A. Ahmad-Khanlou, H.P. Buchkremer and D. Stöver: Vacuum plasma spraying of NiTi protection layers, Mater. Lett. **57** (2002) 647–651.

[23] S. Tria, O. Elkedim, W.Y. Li and H. Liao: Ball milled Ni–Ti powder deposited by cold spraying, J. Alloy. Compd. **483** (2009) 334–336.

[24] G. Mauer, K.-H. Rauwald, Y.J. Sohn and T.E. Weirich: Cold gas spraying of nickel-titanium coatings for protection against cavitation, J. Therm. Spray Technol. **30** (2021) 131–144.

[25] H. Cicek, I. Efeoglu, Y. Totik, K.V. Ezirmik and E. Arslan: A low temperature in-situ crystalline TiNi shape memory thin film deposited by magnetron sputtering, Surf. Coat. Technol. **284** (2015) 90–93.
[26] L. Wang, M. Okugawa, H. Konishi, Y. Liu, Y. Koizumi and T. Nakano: Fusion of Ni plating on CP-titanium by electron beam single-track scanning: Toward a new approach for fabricating TiNi self-healing shape memory coating, Materials **16** (2023) 5449.
[27] L. Wang, M. Okugawa, Y. Liu, K. Cho, H.Y. Yasuda, T. Nakano and Y. Koizumi: NiTi coating formation on Ti for enhanced wear resistance utilizing electron-beam additive manufacturing technique, Surf. Interfaces **72** (2025) 107024.
[28] M. Okugawa, Y. Furushiro, S. Motoyama, Y. Liu, T. Nakano and Y. Koizumi: Integrated computational and experimental study on rapid heating and cooling in powder-bed fusion of Al-Si hypoeutectic alloys, Mater. Trans. **67** (2026), in press.
[29] T. Ishimoto *et al.*: Superimpositional design of crystallographic textures and macroscopic shapes via metal additive manufacturing —Game-change in component design—, Acta Mater. **286** (2025) 120709.
[30] M. Okugawa, K. Saito, H. Yoshima, K. Sawaizumi, S. Nomoto, M. Watanabe, T. Nakano and Y. Koizumi: Solute segregation in a rapidly solidified Hastelloy-X Ni-based superalloy during laser powder bed fusion investigated by phase-field and computational thermal-fluid dynamics simulations, Addit. Manuf. **84** (2024) 104079.
[31] Y. Liu, K. Nose, M. Okugawa, Y. Koizumi and T. Nakano: Fabrication and Process Monitoring of 316L Stainless Steel by Laser Powder Bed Fusion with μ-Helix Scanning Strategy and Narrow Scanning Line Intervals, Mater. Trans. **64** (2023) 1135–1142.
[32] M. Okugawa, Y. Isono, Y. Koizumi and T. Nakano: Raking process for Powder Bed Fusion of Ti-6Al-4V alloy Powder Analyzed by Discrete Element Method, Mater. Trans. **64** (2023) 37–43.
[33] M. Okugawa, D. Izumikawa and Y. Koizumi: Simulations of Non-equilibrium and Equilibrium Segregation in Nickel-based Superalloy Using Modified Scheil-Gulliver and Phase-field Methods, Mater. Trans. **61** (2020) 2072–2078.
[34] N. Cameron and Z. Farhat: Investigation into the wear and dent resistance of Ni/Ti nanolaminates and superelastic NiTi coating, J. Mater. Eng. Perform. **28** (2019) 6033–6041.
[35] T. Abubakar, M. Rahman and J. Stokes: Effect of Annealing Treatment on the Wear Properties of Ni Rich NiTi Alloy Coatings, Adv. Mater. Res. **686** (2013) 192–200.
[36] G. Carlucci, L. Patriarca, A.G. Demir, J.N. Lemke, A. Coda, B. Previtali and R. Casati: Building Orientation and Heat Treatments Effect on the Pseudoelastic Properties of NiTi Produced by LPBF, Shape Mem. Superelast. **8** (2022) 235–247.
[37] J.J. Marattukalam, V.K. Balla, M. Das, S. Bontha and S.K. Kalpathy: Effect of heat treatment on microstructure, corrosion, and shape memory characteristics of laser deposited NiTi alloy, J. Alloy. Compd. **744** (2018) 337–346.
[38] H.Z. Lu, Z.J. Zhou, Y. Yang, R.C. Wang, H.W. Ma, W.S. Cai, D.Z. Zhu and C. Yang: Effect of heat treatment on the microstructure and superelasticity of NiTi alloy via selective laser melting, J. Mater. Res. Technol. **30** (2024) 1044–1055.
[39] Z. Li, J. Cai, Z. Zhao, Y. Yang, Y. Ren, G. Sha, L. Cui, K. Yu, D. Jiang, Y. Xiao, S. Mao and S. Hao: Local chemical inhomogeneity enables superior strength-ductility-superelasticity synergy in additively manufactured NiTi shape memory alloys, Nat. Commun. **16** (2025) 1941.
[40] Denki Kagaku Kai: *Denki Kagaku Benran [Electrochemical Handbook]*, 6th ed., (Maruzen Publishing, Tokyo, 2013).
[41] Thermo-Calc Software, Titanium and TiAl-based Alloys Databases, Version 4 (TCTI4), (2022). https://thermocalc.com/products/databases/ (accessed October 1, 2023).
[42] E.S. Berkovich: The three-faceted diamond pyramid for microhardness testing, Zavod. Lab. **16** (1950) 345.
[43] A. Shimamoto, K. Tanaka, Y. Akiyma and H. Yoshizaki: Nano-indentation of glass with a tip-truncated Berkovich indenter, Philos. Mag. A **74** (1996) 1097–1105.
[44] International Organization for Standardization, Metallic materials — Instrumented indentation test for hardness and materials parameters — Part 1: Test method (ISO Standard No. 14577-1:2015), (2015). https://www.iso.org/standard/56626.html.
[45] J.E. Field: *The Properties of Natural and Synthetic Diamond*, (Academic Press, London, 1992).
[46] B.S. Shariat and Y. Liu: Variation of Poisson's Ratio of NiTi During Pseudoelastic Deformation, Shape Mem. Superelast. **9** (2023) 608–614.
[47] W. Ni, Y.-T. Cheng and D.S. Grummon: Microscopic superelastic behavior of a nickel-titanium alloy under complex loading conditions, Appl. Phys. Lett. **82** (2003) 2811–2813.
[48] ASTM International, Test Method for Linearly Reciprocating Ball-on-Flat Sliding Wear, (2022). https://doi.org/10.1520/G0133-22.
[49] J.F. Shackelford and W. Alexander: *CRC Materials Science and Engineering Handbook*, 3rd ed., (CRC Press, Boca Raton, 2000). https://doi.org/10.1201/9781420038408.
[50] S. Divinski, I. Stloukal, L. Král and C. Herzig: Diffusion of Titanium and Nickel in B2 NiTi, Defect Diffus. Forum **289–292** (2009) 377–382.
[51] A. Babaei-Dehkordi, M. Soltanieh, M. Mirjalili, M. Asherloo and A. Mostafaei: Understanding Interfacial Reactions in Ti–Ni Diffusion Couple, Materials **16** (2023) 2267.
[52] M. Lifshitz and V.V. Slezov: KINETICS OF DIFFUSIVE DECOMPOSITION OF SUPERSATURATED SOLID SOLUTIONS, Sov. Phys. J. Exptl. Theoret. Phys. (U.S.S.R.) **35** (1958) 331–339.
[53] E.E. Timofeeva, N.Yu. Surikov, A.I. Tagiltsev, A.S. Eftifeeva, A.A. Neyman, E.Yu. Panchenko and Yu.I. Chumlyakov: The superelasticity and shape memory effect in Ni-rich Ti-51.5Ni single crystals after one-step and two-step ageing, Mater. Sci. Eng. A **796** (2020) 140025.
[54] R.C.D. Richardson: The wear of metals by relatively soft abrasives, Wear **11** (1968) 245–275.
[55] S. Kikuchi, S. Suzuki and H. Akebono: Microstructural Characterization and Wear Behavior of Sintered Compacts Fabricated from Plasma-Nitrided Commercially Pure Titanium Powder, Mater. Trans. **61** (2020) 2284–2291.
[56] W. Ni, Y.-T. Cheng, M. Lukitsch, A.M. Weiner, L.C. Lev and D.S. Grummon: Novel layered tribological coatings using a superelastic NiTi interlayer, Wear **259** (2005) 842–848.
[57] A. Leyland and A. Matthews: On the significance of the H/E ratio in wear control: a nanocomposite coating approach to optimised tribological behaviour, Wear **246** (2000) 1–11.
[58] B.D. Beake: The influence of the H/E ratio on wear resistance of coating systems – Insights from small-scale testing, Surf. Coat. Technol. **442** (2022) 128272.
[59] Z. Pang, Q. Zeng, Z. Ning, W. He, Z. Wang, J. Wang and L. Li: Ultralow friction and low wear behavior of in-situ formed NiTiO3 from 60NiTi alloy at 350 °C, Intermetallics **168** (2024) 108271.
[60] R. Neupane and Z. Farhat: Wear Resistance and Indentation Behavior of Equiatomic Superelastic TiNi and 60NiTi, Mater. Sci. Appl. **6** (2015) 694–706.
[61] L. Yang, M. Wen, X. Dai, G. Cheng and K. Zhang: Ultrafine Ceramic Grains Embedded in Metallic Glass Matrix: Achieving Superior Wear Resistance via Increase in Both Hardness and Toughness, ACS Appl. Mater. Interfaces **10** (2018) 16124–16132.
[62] K.G. Budinski: *Surface Engineering for Wear Resistance*, (Englewood Cliffs, N.J., Prentice Hall, 1988). http://archive.org/details/surfaceengineeri0000budi (accessed December 30, 2024).
[63] Y.-T. Cheng and C.-M. Cheng: Relationships between hardness, elastic modulus, and the work of indentation, Appl. Phys. Lett. **73** (1998) 614–616.
[64] J.A. Greenwood and J.B.P. Williamson: Contact of nominally flat surfaces, Proc. R. Soc. London, Ser. A **295** (1966) 300–319.
[65] D.Y. Li: A new type of wear-resistant material: pseudo-elastic TiNi alloy, Wear **221** (1998) 116–123.
[66] Z.N. Farhat and C. Zhang: The role of reversible martensitic transformation in the wear process of TiNi shape memory alloy, Tribol. Trans. **53** (2010) 917–926.
[67] H. Vafaeenezhad, S. Aliakbari-Sani, S.H. Seyedein, A. Ghosh and A.R. Eivani: Flow behavior and strain rate sensitivity assessment of γ and γ′ phases in Co–Al–W-based superalloy using experimental and computational approaches, J. Mater. Res. Technol. **18** (2022) 4617–4630.
[68] X.F. Wang, X.P. Yang, Z.D. Guo, Y.C. Zhou and H.W. Song: Nanoindentation characterization of mechanical properties of ferrite and austenite in duplex stainless steel, Adv. Mater. Res. **26–28** (2007) 1165–1170.

[69] Z. Wang, J. Zhang, H.U. Hassan, J. Zhang, Y. Yan, A. Hartmaier and T. Sun: Coupled effect of crystallographic orientation and indenter geometry on nanoindentation of single crystalline copper, Int. J. Mech. Sci. **148** (2018) 531–539.

[70] L. Zhu, B. Xu, H. Wang, C. Wang and D. Yang: Measurement of mechanical properties of 1045 steel with significant pile-up by sharp indentation, J. Mater. Sci. **46** (2011) 1083–1086.

[71] A. Liu, Q. Pan, M. Chen, W. Xu and W. Chen: An investigation on the relationships between hardness, elas- ticmodulus and the work of 7075 aluminium alloy by nanoindentation, J. Phys. Conf. Ser. **2044** (2021) 012106.

[72] X.Y. Li, J.R. Ye and B. Tang: Study of the Ion Nitrided Layer on Ti-6Al-4V substrate, Adv. Mater. Res. **79–82** (2009) 695–698.

[73] M. Liu, Q. Zheng, X. Wang and C. Xu: Characterization of Distribution of Microstructure and Micro-mechanical Properties of Nickel-Based Single Crystal Superalloy Within the Shot-Peened Layer, Met. Mater. Int. **29** (2023) 2257–2286.

[74] M. Zhang, F. Li, B. Chen and S. Wang: Investigation of micro-indentation characteristics of P/M nickel-base superalloy FGH96 using dislocation-power theory, Mater. Sci. Eng. A **535** (2012) 170–181.

[75] J. Nohava, B. Bonferroni, G. Bolelli and L. Lusvarghi: Interesting aspects of indentation and scratch methods for characterization of thermally-sprayed coatings, Surf. Coat. Technol. **205** (2010) 1127–1131.

[76] J.G. La Barbera-Sosa, Y.Y. Santana, M.H. Staia, D. Chicot, J. Lesage, J. Caro, G. Mesmacque and E.S. Puchi-Cabrera: Microstructural and mechanical characterization of Ni-base thermal spray coatings deposited by HVOF, Surf. Coat. Technol. **202** (2008) 4552–4559.

[77] C. Leither, J. Risan, M. Bashirzadeh and F. Azarmi: Determination of the elastic modulus of wire arc sprayed alloy 625 using experimental, analytical, and numerical simulations, Surf. Coat. Technol. **235** (2013) 611–619.

[78] P. Poza, C.J. Múnez, M.A. Garrido-Maneiro, S. Vezzù, S. Rech and A. Trentin: Mechanical properties of Inconel 625 cold-sprayed coatings after laser remelting. Depth sensing indentation analysis, Surf. Coat. Technol. **243** (2014) 51–57.

[79] K.L. Ng, Q.P. Sun, M. Tomozawa and S. Miyazak: Wear behavior of NiTi thin film at micro-scale, Int. J. Mod. Phys. B **24** (2010) 85–93.